Wideband Millimeter-Wave Dual-Mode Dual Circularly Polarized OAM Antenna Using Sequentially Rotated Feeding Technique

Jie Wu, *Student Member, IEEE*, Zhixiang Huang, *Senior Member, IEEE*, Xingang Ren, Wei E. I. Sha, *Senior Member, IEEE*, and Xianliang Wu

***Abstract*—In this letter, a 2 $\times$ 2 wideband bidirectional dual circularly polarized (CP) orbital angular momentum (OAM) antenna array at millimeter-wave frequency is presented, which can be used to generate dual mode simultaneously by the sequential rotation feeding method. The proposed antenna array is composed of four bidirectional radiating dual CP elements that rotate 90° sequentially to each other in the clockwise direction. The antenna element structure consists of two metasurface patch layers that are loaded on the bidirectional cavity-back slot antenna based on substrate integrated waveguide technology. Results indicate that the left-hand circular polarization (LHCP) with a mode $l_{\mathrm{OAM}} = -1$ in the $+z$-direction and right-hand circular polarization (RHCP) with a mode $l_{\mathrm{OAM}} = +1$ in the $-z$-direction, over a wide impedance ($S_{11} < 10$ dB) and 3 dB axial-ratio relative bandwidth of 32.3% from 26 to 36 GHz. An acceptable agreement has been achieved with the comparison between the measurement and simulation results. The proposed antenna provides a method of generating multimode OAM beams for wideband millimeter-wave wireless communication applications.**

***Index Terms*—Dual circularly polarized (CP), dual mode, metasurface, orbital angular momentum (OAM), sequentially rotated feeding.**

I. Introduction

RECENTLY, with the fast development of telecommunication technology, it has called for higher requirements for increasing spectrum resources and improving the efficiency of spectrum utilization in the wireless communication environment. It has been well known that the broadband properties of millimeter-wave (mm-wave) have been extensively explored in fifth-generation (5G) mobile communication [1]–[3]. Besides, orbital angular momentum (OAM) technology attracts increasing attention in the past dozen years due to its mode orthogonality and potential applications in channel capacity expansion and spectrum utilization [4], [5]. Hence, the mm-wave and OAM technologies are of equal importance to improve transmission capacity, there are several reports about the generation methods and theoretical analysis of OAM at the mm-wave band [6]–[8].

Spin angular momentum (SAM) and OAM constitute the angular momentum (AM) of electromagnetic (EM) waves. It should be noted that the SAM is related to the polarization of the EM waves, which has been widely used in radio frequency and mm-wave band. However, it has been until 1992 that Allen *et al.* [9] discovered an OAM beam consisting of spiral phase fronts, described by the phase index $\exp(il\phi)$, where l can take any integer values, which is essentially different from the SAM waves. Initially, OAM was employed to study the transmission characteristics of optical fibers. Specifically, OAM vortex beams with different topological charges can be transmitted and received at the same operating frequency in the optical communication experiment [10]. In 2007, Thidé *et al.* first carried out the numerical simulation of the radio frequency band and put forward the constraint condition of generating OAM beams by using an antenna array [4]. Since then, the approaches for generating and analyzing OAM vortex beams in the radio frequency band have been substantially enriched and developed [11]–[14]. Furthermore, in our previously published work [15] and related literatures [16], [17], the method for generating multiple OAM modes using electrically tunable antenna arrays was proposed, this generation method is flexible to rapidly control and switch between different modes. The operating frequencies in previous works all fall into the microwave band, due to the limited performance of the tunable device and the bias circuit, it is difficult to realize electrically reconfigurable designs in the mm-wave band. Therefore, resolving the challenging topics for multimode, multipolarization, and multifrequency OAM antenna array in the mm-wave band are promising for potential applications in wireless communication prospects.

In this letter, a dual circularly polarized (CP) dual-mode OAM antenna array with sequential rotation feeding (SRF) technique at mm-wave band (26–36 GHz) is presented. The antenna element radiates to both sides through the cavity-backed

Manuscript received March 16, 2020; revised May 2, 2020 and May 19, 2020; accepted May 19, 2020. Date of publication May 25, 2020; date of current version August 4, 2020. This work was supported by the National Natural Science Foundation of China under Grant 61722101, Grant 61701003, and Grant 61971001. *(Corresponding author: Zhixiang Huang.)*

Jie Wu is with the Key Laboratory of Intelligent Computing and Signal Processing, Ministry of Education and the Key Laboratory of Electromagnetic Environmental Sensing, Department of Education of Anhui Province, Anhui University, Hefei 230039, China, and also with the Key Laboratory of Micro-Nano Electronic Devices and Smart Systems of Zhejiang Province, College of Information Science and Electronic Engineering, Zhejiang University, Hangzhou 310027, China (e-mail: wujie@mail.hfut.edu.cn).

Zhixiang Huang, Xingang Ren, and Xianliang Wu are with the Key Laboratory of Intelligent Computing and Signal Processing, Ministry of Education and the Key Laboratory of Electromagnetic Environmental Sensing, Department of Education of Anhui Province, Anhui University, Hefei 230039, China (e-mail: zxhuang@ahu.edu.cn; xgren@ahu.edu.cn; xlwu@ahu.edu.cn).

Wei E. I. Sha is with the Key Laboratory of Micro-Nano Electronic Devices and Smart Systems of Zhejiang Province, College of Information Science and Electronic Engineering, Zhejiang University, Hangzhou 310027, China (e-mail: weisha@zju.edu.cn).

Digital Object Identifier 10.1109/LAWP.2020.2997057

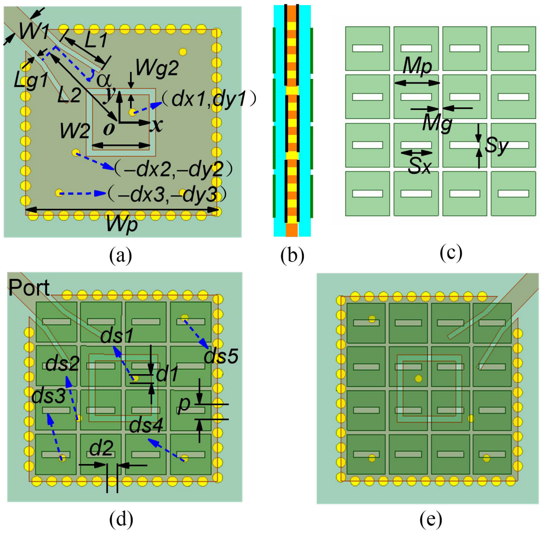

Fig. 1. Configurations of the antenna element. (a) Top view of the SIW-based bidirectional cavity-backed slot. (b) Side view of antenna element A (schematic diagram). (c) Metasurface array of antenna element. (d) Top view of the antenna element A. (e) Bottom view of antenna element A.

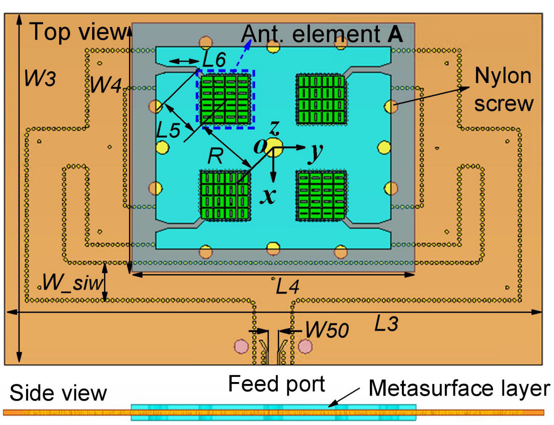

Fig. 2. Configurations of the antenna array (top view and side view).

slots, and the working bandwidth can be effectively expanded by loading the metasurface layer directly above the slot. The proposed OAM antenna array has radiation characteristics of left-hand circular polarization (LHCP) with a mode $l_{\mathrm{OAM}} = -1$ in the $+z$-direction and right-hand circular polarization (RHCP) with a mode $l_{\mathrm{OAM}} = +1$ in the z-direction. The simulation and measurement results of reflection coefficients, gains, 3 dB axial ratio (AR), and phase distributions indicate the effectiveness of the proposed antenna design for generating dual CP dual-mode OAM beam simultaneously in 26–36 GHz band.

II. Antenna Design

A. Element Design

The geometries of OAM antenna element and array are depicted in Figs. 1 and 2, respectively. The antenna array is composed of a substrate integrated waveguide (SIW)-based bidirectional cavity-backed slot antenna array and two metasurface layers, each of which consists of four elements. They are fabricated on a 0.508 mm thick Rogers RT5880 substrate ($\varepsilon_r = 2.2$, $\tan\delta = 0.0009$), and the metasurface layers are stacked on both sides of the SIW-based radiation slot, to achieve a wider operating frequency band. Fig. 1 shows the element structure of the proposed antenna array. By introducing shorting via $ds1$ and $ds2$, which are located at $(dx1, dy1)$ and $(-dx2, -dy2)$, into the SIW-based cavity, a perturbation can be produced. In addition, shorting via $ds3$, which is located at $(-dx3, -dy3)$, $ds4$, and $ds3$ is symmetric about the y-axis, and $ds5$ and $ds4$ are symmetric about the x-axis. Thus, the position of the shorting via $ds1$, $ds2$, $ds3$, $ds4$, and $ds5$ has a great influence on the CP performance of the proposed antenna element and array. Besides, in each element structure, the metasurface consists of 4×4 periodic metal patches with periodicity of $(M_p + M_g)$ and a gap M_g. In order to better control the surface current distribution and improve the circular polarization performance of the antenna, a rectangular slot is added in the center of the metal patch.

The operating frequency is determined primarily by the size of the complementary square split, and its initial value can be calculated by the following formula [18]:

$$W_2 = \frac{\lambda_0}{2\sqrt{\varepsilon_{\mathrm{eff}}}} \tag{1}$$

where λ_0 is the wavelength of the central working frequency in the free space, which can make the square split ring resonating at $\mathrm{TM}_{01}/\mathrm{TM}_{10}$ modes. In order to excite the two orthogonal modes, the initial size of SIW cavity for $\mathrm{TE}_{120}/\mathrm{TE}_{210}$ modes is determined by [19]

$$f_{mnp} = \frac{1}{2\sqrt{\mu\varepsilon}}\sqrt{\left(\frac{1}{L_{\mathrm{eff}}}\right)^2 + \left(\frac{2}{L_{\mathrm{eff}}}\right)^2} \tag{2}$$

$$L_{\mathrm{eff}} = W_3 - 1.08\frac{d_2^2}{p} + 0.1\frac{d_2^2}{W_3} \tag{3}$$

where μ and ε represent the permeability and permittivity of the dielectric substrate, respectively. Furthermore, a finite metasurface can be considered as a cavity, and the resonance of surface waves is governed by the following equation [20]:

$$\beta_{\mathrm{SW}} = \frac{\pi}{4 \times (M_p + M_g)} \tag{4}$$

where β_{sw} represents the propagation constant of surface wave.

The simulated characteristics of the antenna element and array are obtained by using the full-wave simulator software HFSS. The optimized dimensions are: $W_1 = 0.8$, $L_{g1} = 0.2$, $L_1 = 1.8$, $L_2 = 3.8$, $d_{x1} = 0.45$, $d_{y1} = 0.4$, $d_{x2} = 1.75$, $d_{y2} = 1.2$, $d_{x3} = 2.6$, $d_{y3} = 2.8$, $R = 7.2$, $W_2 = 2.2$, $W_{g2} = 0.3$, $M_p = 1.6$, $M_g = 0.16$, $S_x = 1.1$, $S_y = 0.25$, $d_1 = 0.3$, $d_2 = 0.4$, $W_p = 7.2$, $L_3 = 80$, $W_3 = 52.5$, $W_4 = 37$, $L_4 = 42$, $W\_siw = 5.6$, $L_5 = 6.5$, $L_6 = 4.3$, and $W_{50} = 1.4$, unit: mm, $\alpha = 12°$. Simulated reflection coefficient, 3 dB AR, and gains of the element are shown in Fig. 3. It can be clearly observed that both radiation directions have good bandwidth and circular polarization characteristics.

B. Analyses of the OAM Mode

In [13], Zhang and Li theoretically analyzed the mechanism of different modes of OAM vortex waves, which are generated by SRF of CP antenna array. It is well known that the total AM is composed of SAM and OAM (i.e., $j_{\mathrm{AM}} = l_{\mathrm{OAM}} + l_{\mathrm{SAM}}$, where l_{OAM} and l_{SAM} represent modes of SAM and OAM, respectively), in which SAM is generated by the polarization of the antenna. It means that LHCP and RHCP can generate SAM

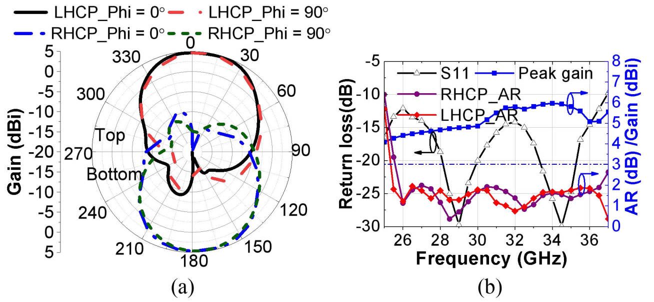

Fig. 3. Simulated results of antenna element. (a) Gains of LHCP and RHCP. (b) Reflection coefficient, 3 dB AR, and peak gain.

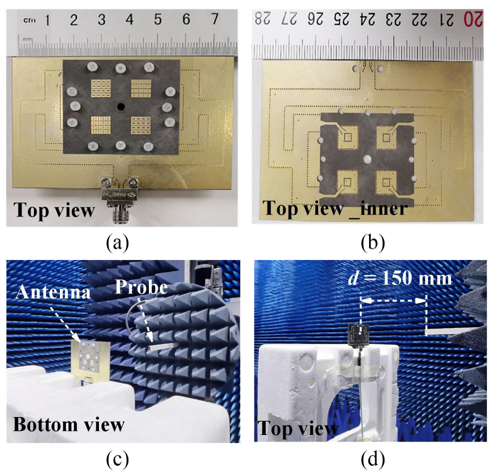

Fig. 4. Fabricated array antenna. (a) Front view. (b) Back view. (c) Bottom view in the anechoic chamber. (d) Top view in the anechoic chamber.

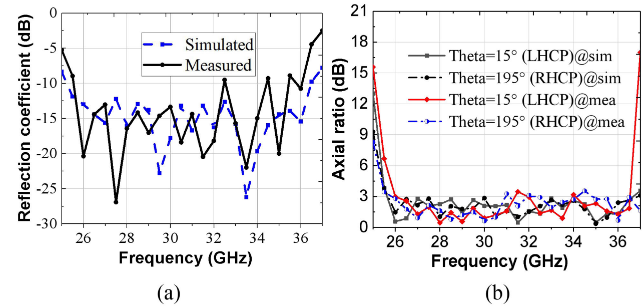

Fig. 5. (a) Measured and simulated reflection coefficient of the antenna array. (b) Measured and simulated AR of the antenna array.

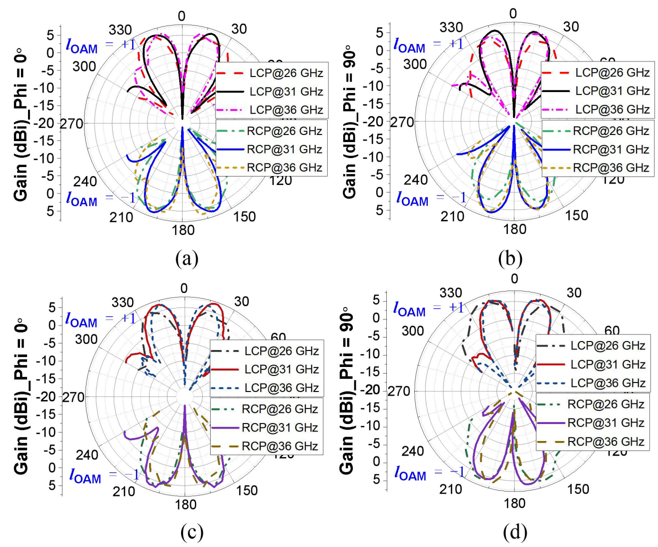

Fig. 6. Far-field radiation of the antenna array at 26, 31, and 36 GHz. (a) Simulated and (c) measured far-field radiation pattern in the *xoz* plane. (b) Simulated and (d) measured far-field radiation pattern in the *yoz* plane.

with $l_{\mathrm{SAM}} = +1$ and $l_{\mathrm{SAM}} = -1$, respectively. As illustrated in Fig. 3, the array consists of four CP antenna elements that radiate in two directions and excite the same amplitude and phase. Two phase-shifting schemes [270, 180, 90, 0] with $l_{\mathrm{OAM}} = -1$ and [0, 90, 180, 270] with $l_{\mathrm{OAM}} = +1$ can be obtained in the $+z$-direction and $-z$-direction by the SRF method, respectively. Based on this, the CP antenna element is different from the linear polarization element, and the total AM pattern cannot be recognized referring to the observed phase distribution. Moreover, the phase distribution of z-components cannot represent the OAM mode due to the existence of SAM information. Furthermore, the phase distributions of x- and y-components are not related to SAM information, but only to OAM.

III. Experiments and Results

A. Reflection Coefficient, Gains, and AR

According to the aforementioned theoretical analysis, the prototype OAM antenna array was then fabricated on the Rogers RT5880 substrate by using commercial high-frequency printed circuit board technology and the measurement setup in microwave chamber, as shown in Fig. 4. The SIW-based bidirectional cavity-backed slot antenna array and two metasurface layers are made of 0.018 mm copper film and fixed together by plastic nuts. The size of the entire fabricated antenna is 80 $\times$ 52.5 $\times$ 1.524 mm^3 (i.e., $8.2\lambda_0 \times 5.4\lambda_0 \times 0.157\lambda_0$, where λ_0 is the central frequency wavelength). Fig. 5 illustrates that the experimental results of reflection coefficients are in good agreement with the simulation results. The results show that the effective -10 dB impedance bandwidth of the proposed OAM antenna is 32.3% from 26 to 36 GHz.

The measured AR properties at the beams (i.e., theta $= 15°$ for $l_{\mathrm{OAM}} = -1$ and theta $= 195°$ for $l_{\mathrm{OAM}} = +1$, respectively) corresponding frequency bandwidth (26–36 GHz) are plotted in Fig. 5(b), where the simulation results in the *xoz* plane are included for comparison. The simulation and measurement gain patterns of the OAM antenna are shown in Fig. 6 at the *xoz* plane and *yoz* plane, respectively. According to Fig. 6(c) and (d), the measured half-power beamwidth of the OAM antenna is listed in Table I. The gain patterns illustrate that the maximum null-depths are -11.4 dBi for $l_{\mathrm{OAM}} = -1$ and -13.9 dBi for $l_{\mathrm{OAM}} = +1$ at different cut-planes, which verifies the donut-shaped intensity distribution of vortex beams. In addition, the CP performances of the two OAM modes in the *xoz* plane and *yoz* plane are also evaluated, respectively, as shown in Fig. 7. It can be conspicuously observed that the characteristic on-axis phase singularities of the OAM are indicated on the AR for both LHCP and RHCP.

B. Measurements of the Field Distribution Results

To further validate the vortex phase information of the OAM modes, the near-field scanning experiments were carried out in

TABLE I
MAIN SPECIFICATIONS OF THE MEASURED GAIN PATTERNS

l_{OAM}	Cut-plane and peak gain (dBi)	Half-power beamwidth	Maximum Null-depth
−1 (LHCP)	*xoz*-plane 6.82	(10° to 24°) (335° to 347°)	-11.4 dBi
	yoz-plane 6.25	(14° to 25°) (337° to 352°)	
+1 (RHCP)	*xoz*-plane 6.56	(154° to 167°) (190° to 206°)	-13.9 dBi
	yoz-plane 6.32	(161° to 172°) (192° to 204°)	

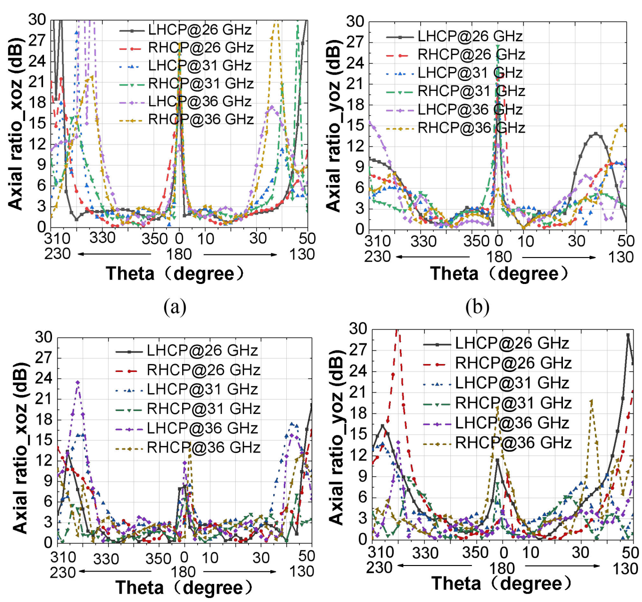

Fig. 7. AR patterns of the antenna array at 26, 31, and 36 GHz. (a) Simulated and (c) measured AR patterns in the *xoz* plane. (b) Simulated and (d) measured AR patterns in the *yoz* plane.

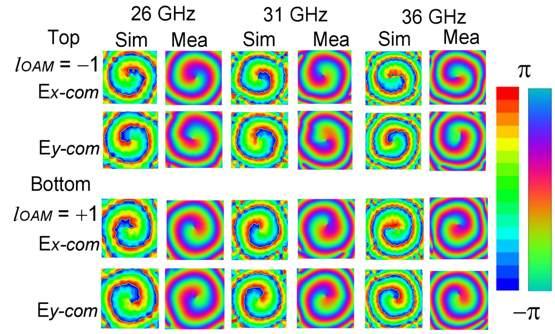

Fig. 8. Simulated and measured phase fronts at 26, 31, and 36 GHz.

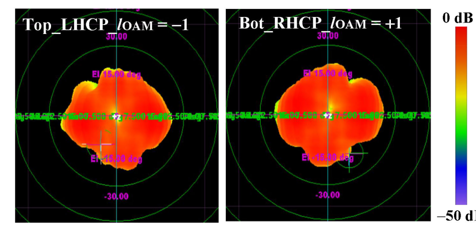

Fig. 9. Measured 3-D radiation pattern at 31 GHz (top view).

a microwave chamber. An open-ended rectangular waveguide is employed as a near-field detector. The distance between the antenna surface and the measuring plane is 150 mm ($15.5\lambda_0$), and the scanning range is 140 mm × 140 mm. Since the near-field scanning can only be carried out in one direction, the $+z$- and $-z$-directions of the antenna need to be measured separately. Furthermore, the spatial phase distributions of the Cartesian components of the electric fields in a square region perpendicular to the propagation direction are observed, as shown in Fig. 8. The x-component and y-component reveal the mode number l_{OAM} of the OAM. Fig. 8 illustrates that the experimental results are in good consistency with the simulated results.

Furthermore, the measured far-field radiations of the OAM antenna for both $+z$-direction with LHCP and $-z$-direction with RHCP are shown in Fig. 9, which are constructed form the near-field measurement platform at a distance of $15.5\lambda_0$ from the antenna surface. The measured results demonstrate that amplitude null can be obtained at the center of the OAM beams, which are the typical characteristics of the doughnut-shaped OAM beams. The purity of these OAM beams generated by the proposed antenna is calculated using the discrete Fourier transform algorithm [21], [22]. The simulated OAM spectrum weight results of $l_{\mathrm{OAM}} = +1(-1)$ at 26, 31, and 36 GHz are calculated to be 50.6%, 48.3%, and 54.4% (49.9%, 50.5%, and 51.8%), respectively. It can be demonstrated that the proposed OAM antenna has a stable purity characteristics over the wide mm-wave band. All the aforementioned simulated and measured results are in good agreement with each other in terms of the CP performance, AR, gain, and phase distributions. Some of the minor differences are due to the processing and testing errors.

IV. CONCLUSION

In this letter, a wideband bidirectional dual CP dual-mode OAM array antenna with SRF has been analyzed, fabricated, and measured. The simulated and experimental results show that the antenna exhibits clear vortex wave characteristics in a wide mm-wave band of 26–36 GHz by using the SRF, in details, the OAM mode in the $+z$-direction is –1 with LHCP, and in the $-z$-direction is +1 with RHCP. The results show that the antenna has the advantages of well circular polarization, gain, and dual mode, which provides a broad application prospect in mm-wave, such as short distance communication, tunnel communication systems, magnetic resonance imaging, etc. If higher order OAM modes are produced, the number of array elements needs to be increased and the feed network needs to be redesigned. However, it can be confirmed that the proposed OAM mode antenna paves a preliminary method to design higher order OAM modes.

REFERENCES

[1] T. S. Rappaport *et al.*, "Millimeter wave mobile communications for 5G cellular: It will work!" *IEEE Access*, vol. 1, pp. 335–349, 2013.

[2] J. Kornprobst, T. J. Mittermaier, and T. F. Eibert, "A millimeter-wave self-mixing array with large gain and wide angular receiving range," *IEEE Trans. Antennas Propag.*, vol. 66, no. 2, pp. 702–711, Feb. 2018.

[3] Q. Wu, J. Yin, C. Yu, H. Wang, and W. Hong, “Low-profile millimeter-wave SIW cavity-backed dual-band circularly polarized antenna,” *IEEE Trans. Antennas Propag.*, vol. 66, no. 12, pp. 7310–7315, Dec. 2017.

[4] B. Thidé *et al.*, “Utilization of photon orbital angular momentum in the low-frequency radio domain,” *Phys. Rev. Lett.*, vol. 99, no. 8, 2007, Art. no. 087701.

[5] O. Edfors and A. J. Johansson, “Is orbital angular momentum (OAM) based radio communication an unexploited area?” *IEEE Trans. Antennas Propag.*, vol. 60, no. 2, pp. 1126–1131, Feb. 2012.

[6] X. Hui *et al.*, “Ultralow reflectivity spiral phase plate for generation of millimeter-wave OAM beam,” *IEEE Antennas Wireless Propag. Lett.*, vol. 14, pp. 966–969, 2015.

[7] W. Cheng, H. Zhang, L. Liang, H. Jing, and Z. Li, “Orbital-angular-momentum embedded massive MIMO: Achieving multiplicative spectrum-efficiency for mmWave communications,” *IEEE Access*, vol. 6, pp. 2732–2745, 2018.

[8] R. Kadlimatti and P. V. Parimi, “Millimeter-wave nondiffracting circular airy OAM beams,” *IEEE Trans. Antennas Propag.*, vol. 67, no. 1, pp. 260–269, Jan. 2019.

[9] L. Allen, M. W. Beijersbergen, R. J. C. Spreeuw, and J. P. Woerdman, “Orbital angular momentum of light and the transformation of Laguerre-Gaussian laser modes,” *Phys. Rev. A*, vol. 45, no. 11, pp. 8185–8189, 1992.

[10] J. Wang *et al.*, “Terabit free-space data transmission employing orbital angular momentum multiplexing,” *Nature Photon.*, vol. 6, no. 7, pp. 488–496, 2012.

[11] Y. Yan *et al.*, “High capacity millimetre-wave communications with orbital angular momentum multiplexing,” *Nature Commun.*, vol. 5, Mar. 2014, Art. no. 4876.

[12] Z. Zhang, S. Q. Xiao, Y. Li, and B. Z. Wang, “A circularly polarized multimode patch antenna for the generation of multiple orbital angular momentum modes,” *IEEE Antennas Wireless Propag. Lett.*, vol. 16, pp. 521–524, 2017.

[13] Y. M. Zhang and J. L. Li, “Analyses and full-duplex applications of circularly polarized OAM arrays using sequentially rotated configuration,” *IEEE Trans. Antennas Propag.*, vol. 66, no. 12, pp. 7010–7020, Dec. 2018.

[14] M. L. Chen, L. J. Jiang, and W. E. I. Sha, “Quasi-continuous metasurfaces for orbital angular momentum generation,” *IEEE Antennas Wireless Propag. Lett.*, vol. 18, no. 3, pp. 477–481, Mar. 2019.

[15] J. Wu, Z. Zhang, X. Ren, Z. Huang, and X. Wu, “A broadband electronically mode reconfigurable orbital angular momentum metasurface antenna,” *IEEE Antennas Wireless Propag. Lett.*, vol. 18, no. 7, pp. 1482–1486, Jul. 2019.

[16] Y. Wang, Y. Du, L. Qin, and B. Li, “An electronically mode reconfigurable orbital angular momentum array antenna,” *IEEE Access*, vol. 6, pp. 64603–64610, 2018.

[17] L. Kang, H. Li, J. Zhou, S. Zheng, and S. Gao, “A mode-reconfigurable orbital angular momentum antenna with simplified feeding scheme,” *IEEE Trans. Antennas Propag.*, vol. 67, no. 7, pp. 4866–4871, Jul. 2019.

[18] J. Hu, Z. C. Hao, and W. Hong, “Design of a wideband quad-polarization reconfigurable patch antenna array using a stacked structure,” *IEEE Trans. Antennas Propag.*, vol. 65, no. 6, pp. 3014–3023, Jun. 2017.

[19] J. Hu, Z. Hao, and Z. Miao, “Design and implementation of a planar polarization-reconfigurable antenna,” *IEEE Antennas Wireless Propag. Lett.*, vol. 16, pp. 1557–1560, 2017.

[20] S. X. Ta and I. Park, “Low-profile broadband circularly polarized patch antenna using metasurface,” *IEEE Trans. Antennas Propag.*, vol. 63, no. 12, pp. 5929–5934, Dec. 2015.

[21] F. Shen, J. Mu, K. Guo, and Z. Guo, “Generating circularly polarized vortex electromagnetic waves by the conical conformal patch antenna,” *IEEE Trans. Antennas Propag.*, vol. 67, no. 9, pp. 5763–5771, Sep. 2019.

[22] F. Shen, J. N. Mu, K. Guo, S. M. Wang, and Z. Y. Guo, “Generation of continuously-variable-mode vortex electromagnetic waves with three-dimensional helical antenna,” *IEEE Antennas Wireless Propag. Lett.*, vol. 18, no. 6, pp. 1091–1095, Jun. 2019.